

Mapping sediment-laden sea ice in the Arctic using AVHRR remote-sensing data: Atmospheric correction and determination of reflectances as a function of ice type and sediment load

Petra Huck^{a,b,*}, Bonnie Light^{c,1}, Hajo Eicken^b, Michael Haller^{a,b,2}

^a *Institut für Meteorologie und Klimaforschung, Universität Karlsruhe (TH), 76131 Karlsruhe, Germany*

^b *Geophysical Institute, University of Alaska Fairbanks, Fairbanks, AK 99775-7320, USA*

^c *Department of Atmospheric Sciences, University of Washington, Seattle, WA 98195, USA*

Received 18 May 2004; received in revised form 8 September 2006; accepted 1 October 2006

Abstract

Exploiting the fact that the spectral characteristics of light backscattered from sediment-laden ice differ substantially from those of clean ice and that sediment tends to accumulate at the ice surface during the first melt season, remote-sensing techniques provide a valuable tool for mapping the extent of particle-laden ice in the Arctic basin and assessing its particulate loading. This study considers two fundamental problems that still need to be addressed in order to make full use of satellite observations for this type of assessment: (i) the effects of the atmosphere on surface reflectances derived from radiances measured by the satellite sensor need to be quantified and ultimately corrected for, and (ii) the spectral reflectance of the ice surface as a function of particle loading and sub-pixel distribution needs to be determined in order to derive quantitative estimates from the at-sensor satellite signal. Here, spectral albedos have been computed for different ice surfaces of variable sediment load with a radiative transfer model for sea ice coupled with an optical model for particulates included in sea ice. In a second step, the role of the atmosphere in modulating the surface reflectance signal is assessed with the aid of an atmospheric radiative transfer model applied to a “standard” Arctic atmosphere and surface boundary conditions as prescribed by the sea ice radiative transfer model. A series of sensitivity studies helps assess differences between top-of-the-atmosphere and true surface reflectance and has been utilized to derive a look-up table for atmospheric correction of Advanced Very High Resolution Radiometer (AVHRR) data over sediment-laden sea ice surfaces. In particular, the effects of solar elevation, viewing geometry, and atmospheric properties are considered. The atmospheric corrections are necessary for certain geometries and surface types. Large discrepancies between raw and corrected data are particularly evident in the derived coverage of clean ice and ice with small sediment loading.

© 2006 Elsevier Inc. All rights reserved.

Keywords: Sea ice; Atmospheric correction; Remote sensing

1. Introduction

Relative to its areal coverage, the Arctic Ocean’s sea ice cover is of disproportionate importance to the Earth’s climate and radiation budget (Curry et al., 1995; Untersteiner et al.,

1990). This critical role is in large part dependent on the large-scale albedo of the summer ice pack (Perovich et al., 2002). Despite its importance, the data base of observations on the albedo evolution of the ice cover during melt season is not as large as required for purposes of effective validation and constraint of model simulations (Curry et al., 2001; Perovich, 1998; Robinson et al., 1992). This is particularly acute for large-scale estimates based on remotely-sensed data. While some of the key processes governing albedo evolution of summer sea ice, such as melting of the snow cover, establishment of a surface scattering layer in bare ice and the growth and shrinkage of low-albedo melt ponds are reasonably well understood

* Corresponding author. Now at Department of Physics and Astronomy, University of Canterbury, Christchurch, New Zealand.

E-mail address: peh26@student.canterbury.ac.nz (P. Huck).

¹ Now at Applied Physics Laboratory, Polar Science Center, University of Washington, Seattle, WA 98105, USA.

² Now at Meteorologisches Institut Hamburg, Universität Hamburg, 20146 Hamburg, Germany.

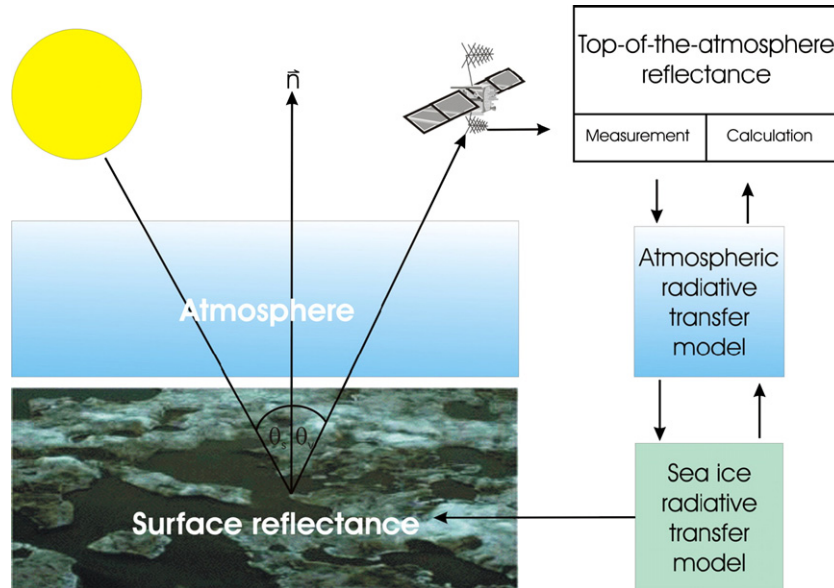


Fig. 1. Simple schematic showing the path for a representative ray in the principal optical plane for a given solar zenith (θ_s) and sensor viewing (θ_v) angle as it emanates from the sun, is backscattered from sediment-laden ice, and detected at the sensor. Also depicted is the relative schematic configuration of the atmospheric and sea ice radiative transfer models, and how they relate to the interpretation and prediction of remotely-sensed reflectance.

(Doronin & Kheisin, 1977; Perovich et al., 2002; Untersteiner et al., 1990), one important characteristic of Arctic sea ice with substantial effects on ice optical properties has not received much attention in this context. As previous study has demonstrated, a substantial fraction of the ice surface (maximum of 40–60% in Chukchi Sea and 0–35% in other areas; Tucker et al., 1999) is covered with sediments in summer, resulting in significant reductions of ice albedo and varying spectral signatures of sea ice in optical remote-sensing data (Light et al., 1998; Reimnitz et al., 1993). Particulates are typically entrained during ice formation over the shallow Arctic shelves and can reach concentrations of more than 1 g l^{-1} in ice formed over the Eurasian Arctic and the Chukchi and Beaufort shelves (Dethleff et al., 1993; Eicken et al., 2000; Osterkamp & Gosink, 1984; Pfirman et al., 1990; Reimnitz et al., 1993; Stierle & Eicken, 2002). Due to surface melt, the sediment accumulates at the surface of multi-year sea ice in the interior Arctic, often concentrated into layers of mud several millimeters thick (Nürnberg et al., 1994; Pfirman et al., 1990).

Owing to the high concentrations of entrained sediments, sediment transport by sea ice constitutes an important component of the overall sediment budget of the Arctic shelves and the Arctic Ocean (Eicken et al., 2000; Pfirman et al., 1990; Reimnitz et al., 1993). However, the patchy distribution and inaccessibility of the Arctic ice pack render quantitative assessments of the total amount of transport difficult. Exploiting the fact that the spectral characteristics of light backscattered from sediment-laden ice differ substantially from those of clean ice (Light et al., 1998) and that sediment tends to accumulate at the ice surface during the first melt season, remote-sensing techniques provide a valuable tool for mapping the extent of particle-laden ice and assessing its particle load (Eicken et al., 2000; Kolatschek, 1998; Reimnitz et al., 1993). While these studies have demonstrated substantial promise in addressing

these problems, and while a new generation of hyper spectral sensors provide data of unprecedented spatial and spectral resolution, two fundamental aspects still need to be addressed in order to make full use of satellite observations: (i) the effects of the atmosphere on the surface reflectances derived from radiances measured by the satellite sensor need to be quantified and ultimately corrected for, and (ii) the spectral reflectance of the ice surface as a function of particle loading and sub-pixel surface type distribution needs to be determined in order to derive quantitative estimates from the at-sensor satellite signal. These issues are independent of the sophistication and complexity of the remote detector.

These two problems are particularly pressing in the context of developing a technique for discerning surface type based on spectral signature. Visible channel AVHRR data have been used to investigate the snow surfaces of Greenland (Stroeve, 2001; Stroeve et al., 1997), the Arctic basin (Jin & Simpson, 2000, 2001), and Antarctica (Winther et al., 2001). Studies using visible channel AVHRR to investigate bare sea ice surfaces have primarily focused on deriving broad-band albedos over Arctic sea ice (DeAbreu et al., 1994; Xiong et al., 2002), and identifying the seasonal cycle of surface albedo (DeAbreu et al., 2001; Lindsay & Rothrock, 1994). However, the use of remotely-sensed optical data to produce accurate estimates of sediment loading relies on the relative magnitudes of backscattered light at different wavelengths and such a measurement is potentially very strongly affected by these two problems. According to Stroeve et al. (1997) corrections as large as 20% can be needed to account for atmospheric disturbance on the reflectance measured on satellite platforms, especially in shortwave bands.

In this study, we address these two problems by considering spectral albedos for different ice surfaces of variable sediment loading computed with a radiative transfer model for sea ice

(Grenfell, 1983, 1991) coupled with an optical model for particulates included in sea ice (Light et al., 1998). The role of the atmosphere in modulating the surface reflectance signal is assessed with the aid of an atmospheric radiative transfer model (6S, Vermote et al., 1997). In particular, effects of solar elevation, viewing geometry, and atmospheric conditions were taken into account. Fig. 1 shows a simple schematic representing the idealized propagation of sunlight backscattered from the ice surface to a satellite receiver and how the two radiative transfer models were used to carry out this work.

A series of sensitivity studies was used to assess differences between top-of-the-atmosphere (TOA) and true surface reflectance and then derive a look-up table for atmospheric correction of Advanced Very High Resolution Radiometer (AVHRR) data over sediment-laden sea ice surfaces. While the scope of this work was necessarily limited to the consideration of a select number of key cases, these nevertheless help identify those variables that most significantly affect the derived reflectances and point the way towards further, more detailed research.

2. Background

Light et al. (1998) developed a model for the vertical distribution of particulate loading based on physical data and spectral albedo observations taken in sediment-laden sea ice in the Eurasian Arctic. This model specifies the sediment concentration as a function of depth and the inherent optical properties of these particulates. Sediment particulates are assumed to be spherical and to have power law size distributions that, for optical purposes, are well represented by an effective radius of 9 μm (Light et al., 1998). This information is used to calculate vertical profiles of spectral absorption and scattering coefficients. Kolatschek (1998) found that by comparing the albedo of a variety of ice types at short and long wavelengths, the ice type can be classified based on surface type and sediment load. These results were used as the basis for this work.

Although the strongly wavelength-dependent volume absorption is the same for bulk ice and ice grains constituting snow, volume scattering by bare sea ice is generally smaller than the volume scattering generated by a snow pack. This results in substantial differences between the reflectance patterns, or bi-directional reflectance distribution functions (BRDF), for bare sea ice and snow surfaces. Because anisotropic reflectance is an intrinsic property of snow and sea ice, their albedos cannot be obtained simply by assuming the albedo is proportional to the reflectance value at a single angular position. Rather, the anisotropic reflectance factor (ARF) specifies the angular dependence of this proportionality.

Perovich (1994) made direct measurements of the ARF for snow covered, bare, and ponded sea ice. His observations were made at zenith angles of 0°, 30°, and 60°, azimuth angles from -180° to +180° at 30° intervals, and solar zenith angles between 50° and 60°, and they indicate ARF values for bare ice for AVHRR channels 1 (0.540 to 0.820 μm) and 2 (0.600 to 1.120 μm) in the nadir viewing direction of approximately 0.82 and 0.73, respectively. Jin and Simpson (1999) used radiative

transfer calculations to predict ARFs of approximately unity for bare sea ice at nadir viewing angles, and they predict considerable departure from unity as the viewing angle increases. However, these calculations contain considerable uncertainty, as the small-scale surface roughness parameters for bare sea ice are highly uncertain, yet are key to this model calculation. Resolving these uncertainties and minimizing errors in assessing the impact of the atmosphere on satellite-measured radiances requires sophisticated studies of the linkages between BRDFs and surface roughness for different ice types. To our knowledge this data is currently not in existence. However, given that sea ice in summer has been shown to be rough on all relevant length scales, we have confined our sensitivity studies to nadir viewing geometries and assumed reflectance to be proportional to albedo. This may limit extrapolation of our results to higher sensor viewing angles, but is not easily resolved in the absence of required data or conclusive model studies. This approach was also used for summer ice by Xiong et al. (2002) where isotropic reflectance and strictly nadir viewing was assumed for the analysis of reflectance data from bare and ponded ice. As outlined in more detail in Section 4 of this study, this limitation has significant impacts on derived reflectances, however, it is not as consequential for the classification approach adopted here (with estimates of maximum errors evaluated below).

3. Approach and methods

Our overall approach was to first model the spectral albedo for a variety of surface conditions. These modeled albedos were then used to help classify the sediment loading associated with AVHRR radiance data. An atmospheric radiative transfer model was then used to test the sensitivity of these data to uncertainties in sensor viewing geometry, solar angle, and atmospheric conditions.

3.1. Modeling surface albedo

We used a four-stream multilayer radiative transfer model (Grenfell, 1991) to calculate surface spectral albedo for clean and sediment-laden bare and ponded ice. An optical model for the vertical profiles of ice structure and inherent optical properties was derived from spectral albedo observations in the Eurasian Arctic (Light et al., 1998). Table 1 summarizes the properties for bare ice. This profile of optical properties applies

Table 1
Vertical structure used in sea ice radiative transfer model for calculating surface albedo of clean and contaminated snow free sea ice during the melt season

Layer #	Thickness (cm)	σ (cm^{-1})	g	n
1	1	3.3	0.89	1.0
2	4	3.9	0.89	1.0
3	20	7.3	0.90	1.3
4	260	4.8	0.92	1.3

Scattering coefficients (σ), asymmetry parameters (g), and refractive indices (n) are for wavelength 500 nm.

to the ice for both clean and contaminated cases, as the addition of suspended particulate material (SPM) is expected to have the effect of increasing the absorption while leaving the scattering unchanged. For each bare ice case, a four-layer model was used with a 1 m thick uppermost layer. Layer thicknesses, scattering coefficients (σ) and asymmetry factors (g) are indicated for the ice constituting each layer. These profiles were derived from data taken when the melt had progressed sufficiently that the uppermost five centimeter layer of the ice where the SPM were entrained were thoroughly deteriorated and quite porous, scattering less light than the higher scattering 20 cm thick layer beneath. Note that the air/ice refractive index boundary is modeled to occur below the uppermost 5 cm.

Ponded ice was also represented in this study. Observations from the Surface Heat Balance of the Arctic Experiment (SHEBA) indicate that the reflectivity of summer melt ponds varies widely. The range of albedos for clean ponds is due primarily to variations in the scattering in the ice underneath the standing water, not necessarily the pond depth. During the course of the SHEBA summer, broad-band pond albedos dropped from the bare ice albedo value to values as low as 0.1. In particular, from 400 nm to 600 nm light pond albedos were observed to be 0.2 to 0.25 larger than dark pond values (Perovich et al., 2002). We chose to model observations made at SHEBA of a light pond and a dark pond. Both ponds were specified to be 0.25 m deep, and to overlie ice with vertically uniform optical properties. The light pond was modeled with underlying ice 1 m thick with $\sigma=0.4 \text{ cm}^{-1}$ and $g=0.92$. The dark pond was modeled with underlying ice 0.50 m thick with $\sigma=0.32 \text{ cm}^{-1}$ and $g=0.92$. These scattering coefficients and asymmetry parameters were chosen for use in the model simulations to produce agreement with specific cases of observed spectral albedo, and result in considerably less backscattering than for bare ice.

For bare, snow free ice, a clean case and a series of cases with particulate concentrations of 25, 50, 75, 100, 200, 300, 400, 500 and 1000 g m^{-3} were specified. Spectral absorption coefficients for the particulate material were taken from Light et al. (1998). For simplicity, particulates were specified to remain evenly distributed in the uppermost 25 cm of the bare ice. For ponded ice, total particulate loadings were concentrated within the uppermost 1 cm of the ice beneath the pond water. This idealized distribution of particulates is clearly an oversimplification, but it permits this study to be carried out such that results are independent of variations in the vertical distribution of SPM. Furthermore, field observations indicate that SPM are spread over a wider vertical range as a result of increases in the porosity of the uppermost decimeters of the ice during solar heating and melting. All albedos were calculated using direct illumination at zenith angle 50° . The results do not vary significantly from albedos calculated for diffuse incident irradiance (as used by Light et al., 1998), but we selected the more appropriate clear sky case for this visible channel remote-sensing application.

The model calculated spectral albedos for bare and ponded ice types are shown in Fig. 2. At wavelengths above 1000 nm, the curves fall on top one another due to a lack of data on the inherent optical properties of SPM at these wavelengths. Values

of σ , g , and n given in Table 1 were used for the bare ice cases. The albedo for the clean ice case has maximum value at 475 nm, and shows substantial backscattering at wavelengths longer than 600 nm. Clean pond albedos also show peak values at 475 nm, but show considerably less backscatter at $\lambda > 600 \text{ nm}$. Pond albedos for $\lambda > 950 \text{ nm}$ are reduced to Fresnel reflection at the surface as strong absorption within the pond eliminates the possibility of light backscattering from the ice beneath the water. The contrast between albedos for ice and ponds at $\lambda > 600 \text{ nm}$ results from the strong wavelength dependence of the absorption of both pure ice and liquid water, and the lack of scattering within the pond itself. This feature makes it possible to discriminate between ice and standing surface water in the retrieval algorithm.

3.2. Remotely-sensed data

Apparent reflectances were derived from AVHRR local area coverage (LAC) data with a 1.1 km ground-projected instantaneous field-of-view for each detector element. For the detection of sediment-laden sea ice, channels 1 (0.540 to 0.820 μm) and 2 (0.600 to 1.120 μm) contain information relevant to the discrimination of sediment-laden ice and were considered in this study. After applying calibration data, radiances were derived from Level 1b data sets and converted to reflectances based on top-of-atmosphere radiative fluxes in the corresponding spectral bands. Potential calibration problems, in particular with respect to AVHRR channel 2, which may vary with time, are difficult to account for in an approach such as this. However, results presented below indicate that the classification hinges mostly on the channel 1 signal and is much less affected by errors in channel 2, except for very high pond fractions, which are only of limited importance in most cases analyzed.

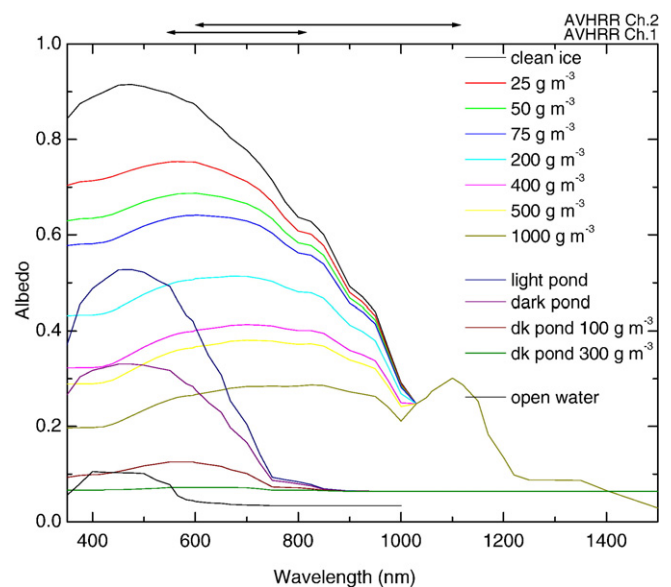


Fig. 2. Modeled surface spectral albedos for bare and ponded ice types under direct incident illumination with solar zenith angle 50° . Total sediment loading is indicated for each curve.

3.3. Atmospheric radiative transfer modeling

The 6S (Second Simulation of the Satellite Signal in the Solar Spectrum) radiative transfer model as coded by Vermote et al. (1997) was employed in this study to simulate the impact of the atmosphere on the sun–target–sensor path as relevant for remote sensing in the visible and near-infrared part of the electromagnetic spectrum (see Fig. 1). The model accounts for absorption as well as multiple Rayleigh scattering by relevant atmospheric constituent gases. Principal absorbing gases include O_2 , O_3 , H_2O , CO_2 , CH_4 , and N_2O . Except for O_3 and H_2O , the rest of the gases are assumed to be uniformly mixed in the atmosphere. The boundary condition at the lower interface is specified by the BRDF for a given surface. The version of the model employed here has been kindly provided by J. Stroeve (National Snow and Ice Data Center, Boulder, Colorado) and integrates BRDFs relevant for different polar snow and ice surfaces (Stroeve et al., 1997). In this study, we only consider Lambertian surfaces, such that the reflectance is proportional to the albedo. This assumption is necessitated by the unknown BRDF of ice surfaces with entrained SPM. Other relevant boundary conditions, such as atmospheric water vapor profiles, are discussed in more detail in the following section. For each radiative transfer calculation, the solar zenith (θ_s) and sensor viewing (θ_v) angles were specified.

4. Results

4.1. Detection of sediment-laden ice

A set of specified surface and atmospheric conditions along with viewing geometry and solar elevation was established as a “base case” and was used for detailed study. This base case was not strongly affected by uncertainties in the surface BRDF and had atmospheric conditions similar to those for the bulk of useful remotely-sensed data. The base case had a nadir viewing sensor, a solar zenith angle of 50° (corresponding to 73.5° latitude at summer solstice), Arctic summertime atmospheric conditions with water vapor and temperature profiles from the SHEBA data set (www.joss.ucar.edu/cgi-bin/codiac/projs?SHEBA), maritime aerosol concentrations as specified by Vermote et al. (1997), and visibility 50 km (Meyer et al., 1991). Reflectances in the spectral bands corresponding to AVHRR channels 1 (ρ_{Ch1}) and 2 (ρ_{Ch2}) of the NOAA-11 satellite were analyzed.

Seventeen different ice, snow, and water surfaces were considered as part of this study. Fig. 3 shows the ratio of reflectances in channel 1 relative to channel 2 (ρ_{Ch1}/ρ_{Ch2}) as a function of ρ_{Ch1} for these 17 cases. These cases include clear, ice-free open water, new snow, melting snow, and ten cases of snow free sea ice with particulate loads ranging from 0 to 1000 g m^{-3} . The largest loadings that were tested are representative of maximum SPM concentrations found in first-year ice (Stierle & Eicken, 2002) and typical for surface accumulations in multi-year ice (Nürnberg et al., 1994). Four different types of ponded ice were also considered and are indicated in Fig. 3, including melt ponds underlain by sediment-

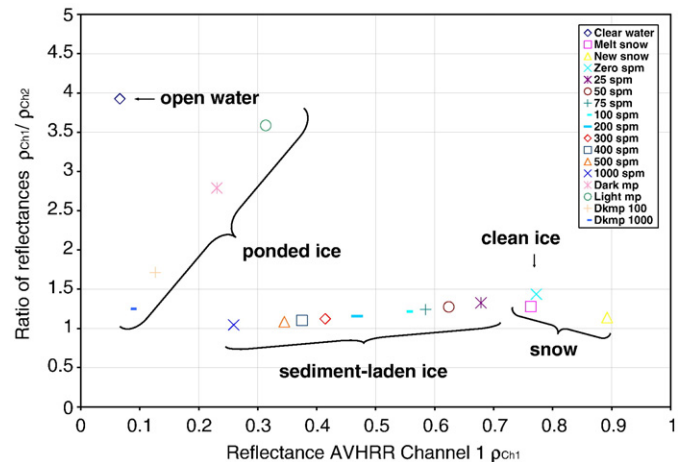


Fig. 3. Ratio of reflectances in channel 1 to channel 2 (ρ_{Ch1}/ρ_{Ch2}) as a function of reflectance in channel 1 (ρ_{Ch1}) for different snow, ice and water surfaces as calculated from the 6S radiative transfer model for the “base case”. Simulations were completed for a wide range of SPM loadings as well as dark and light melt ponds, specified in the legend.

laden ice with SPM concentrations of 100 and 1000 g m^{-3} . The spectral albedos for these different surface types were taken from Fig. 2.

As is evident from the spread of points in Fig. 3, there is a clear dependence of ρ_{Ch1} on the SPM concentration in the uppermost portions of the ice. Due to decreased backscattering by liquid water relative to sea ice, significant absorption of longer wavelength light, (i.e., ρ_{Ch2}), by both pure water and pure ice cause the presence of open water, either completely ice-free or occurring in deeper melt ponds at the surface of sea ice, to shift ρ_{Ch1}/ρ_{Ch2} to values considerably larger than those characteristic of bare ice. In part, the strong sensitivity of ρ_{Ch1}/ρ_{Ch2} may be due to what appears to be an overestimation of this ratio by the 6S code. Based on our sensitivity studies (see more detailed discussion below), this is believed to be the result of a combination of factors, including unrealistically high open water albedos (which include wind-roughened open ocean cases) assumed by the 6S model, along with overestimation of the impacts of water vapor and other atmospheric parameters. The surface albedo simulations summarized in Fig. 2 indicate that a value of ρ_{Ch1}/ρ_{Ch2} below 2 is more realistic and this is borne out by our more detailed analysis in Section 4.2 below. Nevertheless, due to the potential presence of melt water at the ice surface in the form of ponds, varying amounts of sediment loading can be best discriminated by comparing ρ_{Ch1} with the ratio ρ_{Ch1}/ρ_{Ch2} . Here, we extend the approach of Kolatschek (1998) to include a quantitative assessment of the impact of sediment load on ice surface reflectance in spectral intervals relevant for remote-sensing applications as well as a more detailed assessment of the impact of the atmosphere on radiances measured at the satellite sensor.

While a number of factors and sources of error preclude a detailed assessment of sediment load based on a simple regressive relationship, following Kolatschek (1998), we define four different classes of sediment-laden ice: (i) clean or slightly sediment-laden ice, (ii) light, (iii) medium, and (iv) heavy sediment loads. These four classes and two different classes for

ponded ice and one for open water, with their classification boundaries, are designated in Fig. 4. Since this study is concerned with determining sediment loading from AVHRR data in a conservative fashion, the boundaries between different classes aim to minimize the misclassification for sediment-laden ice, while allowing for potentially larger classification errors for non-sediment-laden ice types and open water. Hence, the present classification will likely overestimate the fractions of open water and clean, ponded ice, but this is not deemed problematic within the confined aims of this study.

Errors in AVHRR channel 2 reflectances suggest that there should be significant uncertainties on the classification lines drawn in this figure. In particular, such errors would suggest that horizontal lines in the classification should have significant uncertainty. This will cause errors in the discrimination between bare (both clean and dirty) and ponded (both clean and dirty) ice, but has less effect on the estimation of actual sediment loading. This is particularly true for potential overestimates in ρ_{Ch1}/ρ_{Ch2} as we are excluding heavily ponded ice and open water from further analysis (see also Section 4.2 below).

4.2. Sensitivity studies

Based on the geometry of the AVHRR viewing platform, θ_s for a single AVHRR scene can vary by as much as 5° and θ_v by as much as 7° . We wish to test the sensitivity of our classification technique to appropriate variations in θ_s and θ_v .

For strictly nadir viewing, we varied θ_s in 5-degree steps from 35 to 75° for different surface types in the base case. The results of these simulations are shown in Fig. 5 and show a strong dependence of ρ_{Ch1} on θ_s for clean and sediment-laden ice cases. This dependence is most pronounced for low sediment loadings, where ρ_{Ch1} varies by as much as 0.1. The reverse holds true for open water surfaces and ponded ice, where ρ_{Ch1}/ρ_{Ch2} shows strong dependence on θ_s .

Fig. 6 shows calculations where θ_s is held constant at 50° and θ_v varied at 5° intervals between 0° and 70° . Under these conditions, the sensitivity of ρ_{Ch1} and ρ_{Ch1}/ρ_{Ch2} behave

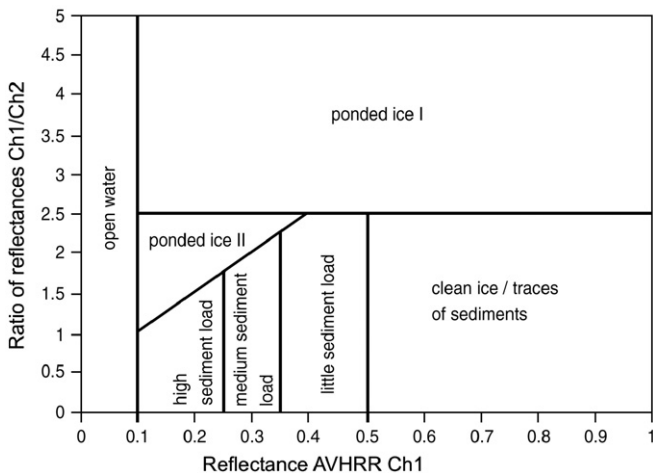


Fig. 4. Classification of four types of sediment loaded ice, two types of ponded ice (clean ponds I and sediment-laden ponds II) and open water.

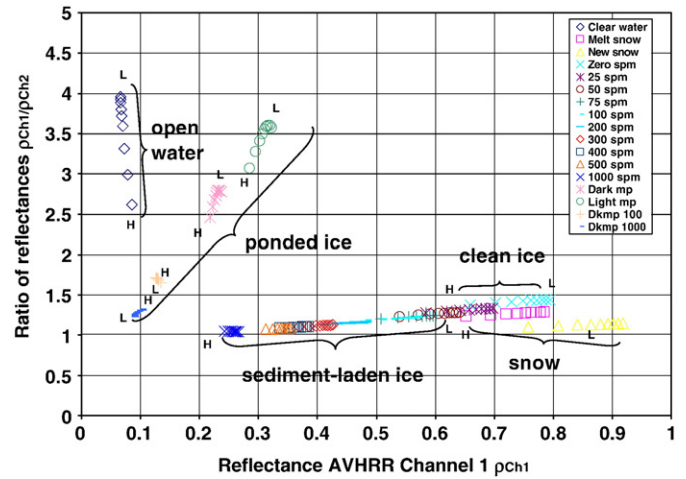


Fig. 5. Dependence of surface reflectance for AVHRR channel 1 (ρ_{Ch1}) and the reflectance ratio of channel 1 to channel 2 (ρ_{Ch1}/ρ_{Ch2}) on variations in solar zenith angle θ_s as determined from atmospheric radiative transfer model simulations. θ_s was varied in 5° intervals with “L” and “H” annotations in the figure indicating the sequence of simulations from lowest (at 35°) to highest (at 75°) solar zenith angle for the spread of data points. Sensor viewing angle was held constant at nadir.

similarly to the sensitivities exhibited in response to changes in θ_s . Increases in θ_v produce large changes in ρ_{Ch1}/ρ_{Ch2} for open water and large changes in ρ_{Ch1} for snow and clean and dirty ice.

The sensitivity studies underscore the fact that both the presence of open water (including in the form of deep melt ponds) and new snow can introduce significant classification errors. New snow is thought to be less of a problem as it is clearly distinguished from clean ice and furthermore during the months of June and July, in particular under clear sky conditions snowfall is not expected to be a significant problem. While the

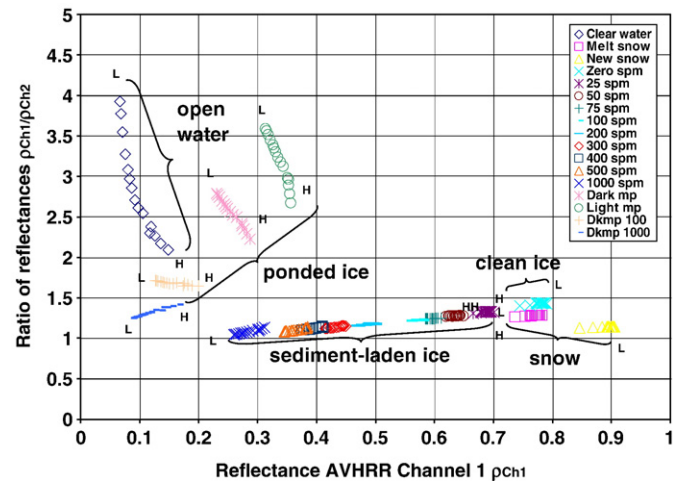


Fig. 6. Dependence of surface reflectance for AVHRR channel 1 ρ_{Ch1} and the reflectance ratio of channel 1 to channel 2 ρ_{Ch1}/ρ_{Ch2} on variations in sensor viewing angle θ_v as determined from radiative transfer model simulations. θ_v was varied in 5° intervals with “L” and “H” annotations in the figure indicating the sequence of simulations from lowest (at 0°) to highest (at 70°) sensor viewing angle. Solar zenith angle is constant at 50° .

classification scheme effectively eliminates open water and heavily ponded ice from the analysis, this approach requires that no mixed-pixels containing two different surface types are analyzed. In the landfast ice case study discussed in Section 4.4 below, we know this to be the case with respect to open water and deeply ponded ice. However, in cases where it is not possible to exclude contamination by open water, such as in the marginal ice zone where floe sizes are generally small, it may be necessary to determine the fraction of open water and deep ponds using other remote-sensing observations and then correcting for the presence of open water through application of a linear mixing model that accounts for the areal fraction of open water. In the absence of such independent data, it may be possible in theory to separate out the fractions of open water and sediment-laden ice based on their different ρ_{Ch1} and ρ_{Ch1}/ρ_{Ch2} signatures. However, uncertainties and errors in determination of the endmember tie points may render such an approach impractical.

The sensitivity of derived reflectances to other variables, including variations in the atmospheric temperature and water vapour profile (several profiles over the Arctic summer measured during the SHEBA experiment have been tested), visibility, and slight differences in band width and center-frequency for different AVHRR sensor types, was assessed.

Table 2
Correction coefficients *a* and *b* for channel 1

		Solar zenith angle in deg. →									
		35	40	45	50	55	60	65	70	75	
a.	0	1.083	1.091	1.101	1.115	1.133	1.159	1.198	1.260	1.369	
	5	1.083	1.091	1.115	1.115	1.134	1.160	1.199	1.261	1.369	
	10	1.084	1.092	1.102	1.116	1.135	1.161	1.200	1.262	1.370	
	15	1.086	1.094	1.104	1.118	1.136	1.163	1.202	1.264	1.372	
	20	1.088	1.096	1.107	1.120	1.139	1.165	1.205	1.376	1.376	
	25	1.092	1.100	1.110	1.124	1.143	1.169	1.208	1.271	1.380	
	30	1.097	1.104	1.115	1.129	1.147	1.174	1.213	1.276	1.386	
	35	1.103	1.111	1.121	1.135	1.154	1.181	1.220	1.283	1.393	
	40	1.111	1.118	1.129	1.143	1.162	1.189	1.229	1.292	1.403	
	45	1.121	1.129	1.140	1.154	1.173	1.200	1.240	1.304	1.416	
	50	1.135	1.143	1.154	1.168	1.187	1.215	1.255	1.320	1.433	
	55	1.154	1.162	1.173	1.187	1.207	1.235	1.276	1.342	1.457	
	60	1.181	1.189	1.200	1.215	1.235	1.263	1.306	1.372	1.490	
	65	1.220	1.229	1.240	1.255	1.276	1.306	1.349	1.418	1.539	
70	1.283	1.292	1.304	1.320	1.342	1.372	1.418	1.490	1.617		
b.	0	-0.018	-0.017	-0.017	-0.019	-0.021	-0.026	-0.032	-0.043	-0.061	
	5	-0.021	-0.021	-0.020	-0.021	-0.023	-0.027	-0.034	-0.044	-0.063	
	10	-0.023	-0.024	-0.024	-0.024	-0.026	-0.030	-0.036	-0.047	-0.065	
	15	-0.025	-0.026	-0.028	-0.029	-0.030	-0.034	-0.040	-0.050	-0.069	
	20	-0.028	-0.029	-0.031	-0.034	-0.036	-0.039	-0.045	-0.056	-0.076	
	25	-0.031	-0.033	-0.034	-0.038	-0.043	-0.047	-0.052	-0.063	-0.084	
	30	-0.036	-0.037	-0.039	-0.043	-0.048	-0.055	-0.063	-0.073	-0.095	
	35	-0.043	-0.043	-0.045	-0.049	-0.054	-0.062	-0.074	-0.089	-0.111	
	40	-0.043	-0.052	-0.052	-0.057	-0.063	-0.071	-0.105	-0.105	-0.134	
	45	-0.045	-0.052	-0.064	-0.066	-0.073	-0.083	-0.097	-0.121	-0.161	
	50	-0.049	-0.057	-0.066	-0.082	-0.087	-0.098	-0.115	-0.141	-0.188	
	55	-0.054	-0.063	-0.073	-0.087	-0.108	-0.118	-0.138	-0.170	-0.222	
	60	-0.062	-0.071	-0.083	-0.098	-0.118	-0.149	-0.169	-0.208	-0.273	
	65	-0.074	-0.085	-0.097	-0.115	-0.138	-0.169	-0.220	-0.262	-0.344	
70	-0.088	-0.105	-0.121	-0.141	-0.170	-0.208	-0.261	-0.353	-0.449		

Table 3
Correction coefficients *a* and *b* for channel 2

		Solar zenith angle in deg. →									
		35	40	45	50	55	60	65	70	75	
a.	0	1.121	1.127	1.135	1.146	1.160	1.180	1.210	1.257	1.337	
	5	1.122	1.128	1.136	1.146	1.160	1.181	1.210	1.257	1.337	
	10	1.122	1.128	1.136	1.147	1.161	1.181	1.211	1.258	1.338	
	15	1.124	1.130	1.138	1.148	1.163	1.183	1.212	1.259	1.339	
	20	1.126	1.132	1.140	1.150	1.164	1.185	1.214	1.261	1.341	
	25	1.128	1.134	1.142	1.153	1.167	1.187	1.217	1.263	1.344	
	30	1.132	1.138	1.146	1.156	1.170	1.191	1.220	1.267	1.347	
	35	1.136	1.142	1.150	1.161	1.175	1.195	1.225	1.272	1.352	
	40	1.142	1.148	1.156	1.167	1.181	1.201	1.231	1.278	1.358	
	45	1.150	1.156	1.164	1.174	1.189	1.209	1.239	1.285	1.367	
	50	1.161	1.167	1.174	1.185	1.199	1.219	1.249	1.296	1.378	
	55	1.175	1.181	1.189	1.199	1.214	1.234	1.264	1.311	1.393	
	60	1.195	1.201	1.209	1.219	1.234	1.254	1.284	1.332	1.414	
	65	1.225	1.231	1.239	1.249	1.264	1.284	1.315	1.363	1.446	
70	1.272	1.278	1.285	1.296	1.311	1.332	1.363	1.412	1.497		
b.	0	-0.0125	-0.011	-0.011	-0.012	-0.013	-0.015	-0.0187	-0.025	-0.036	
	5	-0.0145	-0.014	-0.013	-0.013	-0.014	-0.0158	-0.0192	-0.025	-0.036	
	10	-0.0156	-0.016	-0.016	-0.015	-0.016	-0.0171	-0.0204	-0.026	-0.036	
	15	-0.0169	-0.018	-0.019	-0.019	-0.018	-0.0194	-0.0223	-0.259	-0.038	
	20	-0.0191	-0.019	-0.02	-0.022	-0.023	-0.023	-0.0253	-0.031	-0.041	
	25	-0.0211	-0.022	-0.023	-0.024	-0.027	-0.0283	-0.0301	-0.035	-0.046	
	30	-0.0205	-0.022	-0.023	-0.024	-0.026	-0.0284	-0.0305	-0.033	-0.039	
	35	-0.0292	-0.027	-0.029	-0.031	-0.034	-0.0381	-0.0445	-0.052	-0.063	
	40	-0.0271	-0.035	-0.033	-0.036	-0.039	-0.0434	-0.0508	-0.062	-0.078	
	45	-0.0292	-0.033	-0.042	-0.041	-0.045	-0.0513	-0.0586	-0.072	-0.095	
	50	-0.0314	-0.036	-0.041	-0.053	-0.052	-0.0601	-0.0702	-0.084	-0.111	
	55	-0.037	-0.039	-0.045	-0.052	-0.068	-0.0704	-0.0837	-0.103	-0.132	
	60	-0.0381	-0.043	-0.051	-0.06	-0.071	-0.0933	-0.1004	-0.125	-0.165	
	65	-0.0445	-0.051	-0.059	-0.07	-0.084	-0.1004	-0.1362	-0.155	-0.207	
70	-0.0515	-0.062	-0.072	-0.084	-0.103	-0.1252	-0.1547	-0.218	-0.267		

Xiong et al. (2002) found that in particular for AVHRR channel 2 uncertainties in the water vapor profile can account for as much as 15–25% uncertainty in derivation of broadband albedo, with an uncertainty below 5% for channel 1. Here, we observed that within the range of temporal and spatial variations characteristic of the Arctic, none of the aforementioned parameters (when examined in conjunction) affected the classification of bare and sediment-laden ice to a significant degree and they have hence not been considered further.

A rather surprising factor is that Arctic haze does not have any significant impact on the sensitivity of the reflectances. In the 6S code, users specify either the assumed visibility in km or the aerosol optical depth at 550 nm. We chose to specify the visibility and looked at different values from 10 to 100 km in 10 km steps. It showed that the ρ_{Ch1} versus ρ_{Ch1}/ρ_{Ch2} relationship was affected by the change in visibility only for the open water cases. Meyer et al. (1991) state that a visibility of 45 km is often observed during Arctic spring. It can go down to 12 km during Arctic haze but that still did not affect the classification of snow and ice surfaces in the sensitivity studies. Furthermore, we note that Arctic haze is mostly confined to the months of December through April, with maximum impact in March and early April (Barrie, 1986; Shaw, 1995). With changes in atmospheric stability

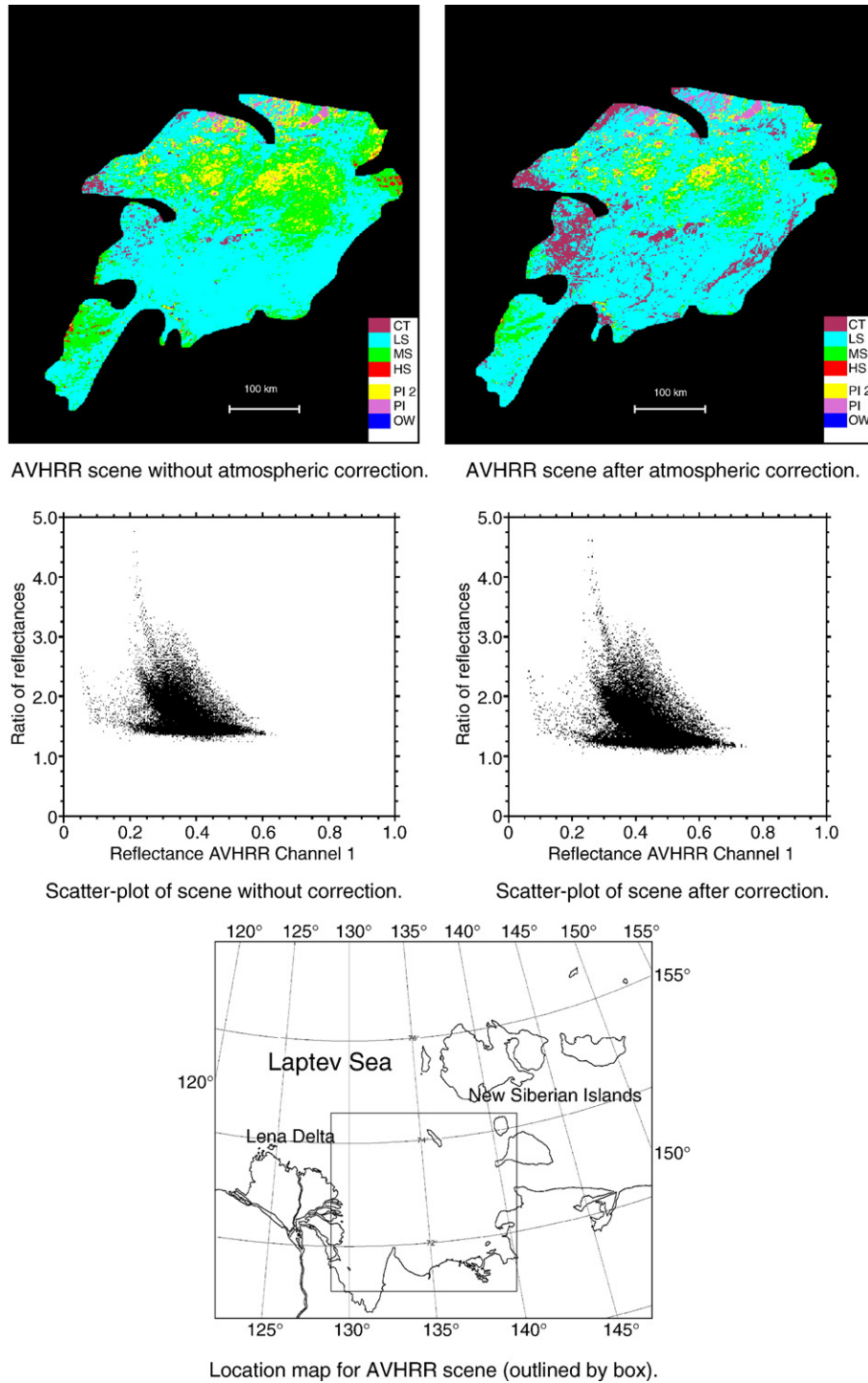


Fig. 7. Example scene (30 June 2000) before and after atmospheric correction, along with corresponding scatter diagrams as applied to sediment-laden ice classification (blue — open water, yellow/orchid — ponded ice I/II (clean/sediment-laden pond, see Fig. 4), maroon — clean ice/traces of sediments, cyan/green/red — light/medium/high sediment load). (For interpretation of the references to colour in this figure legend, the reader is referred to the web version of this article.)

and warming, Arctic haze abates to background aerosol levels from May onwards (Barrie, 1986; Shaw, 1995).

4.3. Atmospheric correction of AVHRR data

As demonstrated by the model simulations and sensitivity studies in the preceding sections, estimating the proportion of

sediment-laden ice over polar sea-ice surfaces requires atmospheric correction of reflectance data. Given the general lack of relevant atmospheric data for specific locations and overflights, and considering the moderate sensitivity and limited variation in the critical atmospheric variables for clear-sky, early to mid-summer conditions which are of relevance in the study of sediment-laden ice, we propose a generalized approach to

Table 4
Areas of different surface types with or without atmospheric correction shown in Fig. 7

Total area: 111,454 km ²			
Surface type	Area without atmospheric correction (km ²)	Area after atmospheric correction (km ²)	Ratio of corrected area to uncorrected area
High load	744.15	209.33	0.3
Medium load	30,830.80	12,665.07	0.4
Light load	67,792.67	78,682.67	1.2
Clean/trace	1,831.73	11,985.05	6.5
Ponded — clean	8,669.65	5,465.57	0.6
Ponded — SPM	1,512.5	2,390.96	1.6
Open water	73.81	54.45	0.7

atmospheric correction of reflectance data. This approach is similar to the way that atmospheric correction has been accomplished for other remote-sensing applications such as the retrieval of land surface reflectances (Liang et al., 2001) or the determination of ocean color (Deschamps et al., 1983). While certain simplifications associated with such a general approach have been retained, with previous work suggesting that such simplifications are acceptable, in particular over high-reflectance surfaces, in contrast to studies of ocean color in the presence of open-ocean marine-type aerosols, e.g., Antoine and Morel (1999) or Sturm and Zibordi (2002), this approach does consider the effects of atmospheric transmittance of diffuse radiation as well as interactions between molecular and aerosol scattering.

Based on the model simulations shown above, plus intercomparison of simulations with and without atmospheric correction, we are now in a position to estimate the effects of the atmosphere in the at-sensor radiances that form the basis of the algorithm for deriving sediment loads in sea ice outlined in the previous section. For most applications of reflectance data over Arctic sea ice, it is sufficient to assume a single standard atmosphere and merely determine a set of simple linear transformation equations,

$$\rho_{\text{sens}} = a\rho_{\text{surf}} + b,$$

that map the surface reflectance ρ_{surf} to the apparent, top-of-the-atmosphere reflectance ρ_{sens} for different solar zenith and sensor zenith angles θ_s and θ_v . The coefficients a and b are tabulated as a function of θ_s and θ_v in Tables 2 and 3 for AVHRR channels 1 and 2, respectively. The largest magnitude of the correction factor a is attained at low solar elevations and high sensor zenith angles. At intermediate sensor and solar zenith angles, the impact of the atmosphere accounts for a difference between a few percent to at most 10% with albedos ranging between 0.5 and 0.9.

Since this lookup table is the product of a rather simplistic approach, it is therefore limited by certain conditions. Atmospheric conditions are restricted to Arctic summer months (June–August) and cloud free scenes are required. Since this lookup table has only been constructed for certain viewing geometries it is not certain that it can be applied to more general viewing conditions. Another potential limitation is our reliance on a limited set of atmospheric profiles, derived from the

SHEBA experiment. As pointed out by Xiong et al. (2002), in particular better information about atmospheric water vapor profiles can result in significant reduction of errors in broadband albedo retrievals and while this is not quite as relevant in the context of the two-channel classification algorithm, it still points towards a need of more realistic atmospheric profile data.

Another potentially significant source of error derives from the lack of specific BRDF data for sediment-laden ice. The maximum extent of the potential classification error can be estimated based on observed and modeled BRDF values for snow surfaces, assuming that the classification is mostly impacted by errors in the magnitude of the channel 1 reflectance. Comparison of field data and modeling (Jin & Simpson, 2000; Perovich, 1994) has shown that modeling tends to under-represent derived sediment-loading or number of misclassified pixels between 10 and 30% for maximum range of solar and sensor zenith angles and homogeneous distribution of ice types.

As shown in Figs. 5 and 6, the effect of the atmosphere on reflectances and reflectance ratios employed in classification of sediment-laden ice depends strongly on the solar elevation and viewing angle. Some sun-satellite configurations may not require atmospheric correction other than a simple transformation of the entire data set (for locally confined data at suitable solar zenith angles). However, due to frequent cloudiness during the Arctic summer, and the often substantial size of the study areas, atmospheric correction of the entire scene will likely be required. Here, based on the coefficients supplied in Tables 2 and 3, a computationally efficient correction can be applied where values of a and b are selected for each pixel in an AVHRR scene.

4.4. Mapping sediment-laden sea ice: a case study in the central Siberian Arctic

By applying the techniques outlined above, we have derived the distribution of sediment-laden ice for a scene within the eastern Laptev Sea in the central Siberian Arctic (Fig. 7 and Table 4). This region has been identified as an important source area for sediment-laden ice (Eicken et al., 2000; Pfirman et al., 1997), with sediment entrainment into sea ice favored by low water depths and a high likelihood of sediment resuspension due to tidal currents and wind mixing (Eicken et al., 2000). While field observations from this area are limited, they confirm high local concentrations of sediment-laden ice (Anderson, pers. comm.; Dethleff et al., 1993; Eicken et al., 2000). Another major advantage for using this region as a test site is the near-complete lack of open water due to the presence of landfast ice throughout the area. This is confirmed by the classification for a scene from 30 June 2000, which indicates around 50 km² of open water (Table 4), most likely deep melt ponds and possibly cracks or openings along the shoreline. The results of the classification for the 30 June scene are shown in Fig. 7.

Table 4 shows the computed areas for the uncorrected and corrected scene in Fig. 7. The ice type with the largest change in area as a result of the correction is the clean ice/trace loading surface type, with an increase in area by a factor of 6.5 after the atmospheric correction was applied. While this increase is significant, the magnitude of this difference is in large part

explained by the fact that in the raw scene very little unponded clean ice has been identified. With the location of the class boundary chosen so as to minimize classification errors for sediment-laden ice, even a small shift of channel 2 radiances results in a significant relative increase in clean ice area. However, overall these numbers are still small compared to ponded or sediment-laden ice. The estimated area of heavily sediment loaded ice changed the least as a result of the correction. In discussing the areas of different ice types, it needs to be kept in mind that potential calibration errors of AVHRR channel 2 may add to the classification error. However, as outlined in more detail above, the sensitivity studies clearly demonstrate that classification results are much more sensitive to changes in channel 1 radiances, which are associated with a much smaller calibration error.

In mapping sediment-laden ice, scenes should be obtained for which the snow cover has completely melted away with some melt of surface ice layers resulting in concentration of sediments in the surface layers. This is typically the case from early to mid-June onwards well into the month of July. Later season images are less desirable because of substantial thinning of the ice and the corresponding decrease in albedo. With such a comparatively narrow window in time and persistent cloud cover, typically only a few suitable scenes can be obtained for any given year in the study area, with substantial portions of the region having to be masked out for cloud cover (as in Fig. 7). The distribution of sediments shown in Fig. 7 is in line with the limited field observations available for this region, showing sediment-laden ice prevalent in the coastal, near-shore areas (in particular off the major river deltas, such as the Lena Delta) and the northeastern regions of the study area, where strong tidal currents and low water depths exist towards the New Siberian Islands (Eicken et al., 2000).

Overall the impact of the atmospheric correction scheme is to reduce the area of high and medium sediment-load ice while increasing that of light sediment-load and clean ice (Table 4). This is evident from the scatter plots of band ratios for $\rho_{\text{Ch1}}/\rho_{\text{Ch2}}$ plotted vs. ρ_{Ch1} where there is a general shift in the ice reflectances towards higher values of ρ_{Ch1} .

One of the few data sets available for validation of the approach is that of Dethleff et al. (1993), who sampled sea ice at a few selected locations in the southeastern Laptev Sea in spring of 1992. They reported overall low sediment loading (mostly between <10 and 100 mg l^{-1}) in the landfast ice which agrees well with satellite-derived maps for that year indicating no highly sediment-laden ice, $<0.3\%$ medium sediment load, 65% light sediment load, and 33% clean ice.

5. Discussion

We have described an approach (following Kolatschek, 1998) to map the distribution of sediment-laden Arctic sea ice based on the impact of particulate inclusions at various concentrations on optical properties of the ice and hence surface reflectance. Simple assessments of this, both in this study and in Kolatschek (1998) and Eicken et al. (2000), indicate that this method holds considerable promise and

reliably distinguishes between different forms of sediment-laden and clean sea ice. For homogeneous, pure endmember ice surfaces present within a given pixel, modeling and a sensitivity study indicate a complete separation between the different prevailing ice surfaces (Fig. 3). What is not clear at present, is how variations in the vertical distribution and types of sediments impact the bulk optical properties of the ice. Based on earlier modeling studies (Light et al., 1998) and what is known about the composition and distribution of sediment-laden ice in the Arctic (Nürnberg et al., 1994) it appears that the greatest source of error is the vertical SPM profile in the ice. Thus, in the later stages of melt, sediments tend to accumulate in optically opaque surface layers (Nürnberg et al., 1994), which may preclude a more detailed distinction between different sediment loadings. While model simulations (Light et al., 1998) suggest that these changes in vertical distribution result in changes in surface reflectance, frequent and dense cloud cover cause difficulties in monitoring these time-dependent late-summer changes from satellite based sensors. However, a field study of changes in optical properties of sediment-laden sea ice undergoing melt may be quite useful in estimating the relative importance of this process. This would be particularly useful for considering spatial and temporal changes in the inherent optical properties of SPM. These quantities have been held fixed in this study, as we are not aware of information about their evolution.

The other major uncertainty with respect to the distribution of sediments is the horizontal inhomogeneity of sediment concentration. Typically, sediment-laden ice has a patchy occurrence at the spatial scales relevant for satellite remote-sensing (Stierle & Eicken, 2002). However, the near-linear dependence of reflectance on sediment loading up to SPM concentrations of several hundred mg l^{-1} suggests that sub-pixel scale mixing effects may not be as critical as vertical variability. Of greater importance is the distribution of melt ponds on the ice surface. Due to the higher absorption in the near-IR (AVHRR channel 2), the presence of a liquid water layer has the tendency to shift values towards higher ratios of $\rho_{\text{Ch1}}/\rho_{\text{Ch2}}$ while at the same time lowering the overall magnitude of ρ_{Ch1} (Fig. 3). Here, this impact on the reflectance signal has been taken into account by only considering data points with low $\rho_{\text{Ch1}}/\rho_{\text{Ch2}}$ values for the mapping of sediment-laden ice. However, as suggested by the area fractions of ponded ice (Table 4) which in many cases are lower by as much as a factor of 2–4 than those expected on level landfast ice, the presence of ponds at the sub-pixel scale may still impact measurements to some extent. The error due to this effect will be small in the early melt season when pond albedos are comparatively high (0.5–0.6) and area fractions still modest (0.1–0.2), but may result in more substantial misclassifications later in the season as ponds deepen, drop in albedo (0.1–0.2), and increase in area fractional coverage (>0.2) (Perovich et al., 2002).

While we did not explicitly calculate the effects of sub-pixel ponding and open water on this classification scheme, we used the points in Fig. 3 to estimate some of these effects and their associated errors. An obvious misclassification of sediment loading would result from the case where a pixel contains clean ice and melt ponds, but no sediment. For melt pond fractional

coverage between 50% and 72% the classification scheme would erroneously produce a light sediment load result, when in reality the ponded ice was clean. Such large pond coverage may not be physically realistic for the central Arctic, but may in fact be observed at the margins of the basin and over increased areas under conditions of intense summer melt and regional ice retreat. As discussed in Section 4.1, other approaches to minimize the impact of mixed-pixel effects would include independent determination of open water or pond fractions.

The analysis of data of higher spatial and spectral resolution, in particular MODIS, may prove useful in helping to correct for this effect. However, field measurements are required as well, since the overall impact of ponds on surface reflectance is poorly understood (Tschudi et al., 2001).

A number of studies have shown soot to have a significant impact on the optical properties of snow and ice (e.g., Warren, 1984). Hence, the question can be raised whether the potential presence of soot would have an impact detectable by remote-sensing methods discussed here. As Grenfell et al. (2002) were able to show, concentrations of soot in snow of offshore Arctic sea ice are too low to have a detectable impact on optical properties, except for the immediate (<500 m) vicinity of a ship stationary over periods of months. At the same time, even higher concentrations reported for coastal locations (see Grenfell et al., 2002, for details) are still 6 orders of magnitude lower than background concentrations of particulates (sediment and biogenic particles) in sea ice, and the impact of other particulates is deemed to outweigh that of soot in almost all locations. This is particularly true for the period of observation of sediment-laden sea ice, after complete removal of snow cover and accumulation of sedimentary and biogenic impurities at the surface of the ice.

Further limitations of this approach can be attributed to the use of the 4-stream radiative transfer modeling. The 4-stream model has been documented to produce accurate estimates of albedo (providing it is fed appropriate inherent optical properties), but is incapable of simulating the BRDF for sea ice and snow surfaces. Data on the BRDF for sea ice, particularly sediment-laden melting sea ice, and the ability to model its angle-resolved reflectance would enhance this effort considerably.

As shown in Section 4.3, the influence of the atmosphere can have a substantial impact on derived reflectances and deduced sediment concentrations. The outlined approach in correcting for the effects of the atmosphere as a function of solar zenith and sensor viewing angle helps diminish the ensuing errors.

6. Conclusions

The high spatial and temporal variability of sediment entrainment within Arctic sea ice has generally rendered previous, field-based research of the phenomenon somewhat inconclusive as to the importance of the process in various regions and various years. As demonstrated by the combination of radiative transfer model simulations and analysis of AVHRR satellite data, remote sensing of sediment-laden ice holds

significant promise and can help overcome problems associated with the significant spatial inhomogeneity observed in sediment loading and the fact that it occurs in largely inaccessible parts of the world's oceans.

Radiative transfer modeling has been employed to develop a classification scheme that uses reflectances in AVHRR channels 1 and 2. This scheme distinguishes between different degrees of sediment loading and the presence of water on the surface of the ice. While the scheme allows for full discrimination between all major ice types for uniform surfaces, variations in the vertical and lateral distribution of sediments as well as patchiness at the sub-pixel level may result in significant errors. Further work is required to separate these different effects and their impact on the reflectance signature. In this context, modern hyperspectral sensors may prove useful as well through improvements in the number and spectral resolution of channels in the visible range. However, at the same time, interpretation of such data sets also requires an improved understanding of some of the shortcomings discussed below as well as more involved data processing.

Atmospheric correction plays an important role in remote sensing. In the Arctic, the applied correction depends highly on the measurement geometry and the surface properties, as has been shown in Section 4. Mapping sediment-laden sea ice in the Arctic can be improved by taking atmospheric influence into account. In particular for some of the sediment-laden ice types found in the Arctic, remote-sensing signatures are strongly impacted by a number of atmospheric variables, resulting in errors if uncorrected. The 6S radiative transfer model is well suited to calculate the impact of atmospheric processes on remote sensing, especially due to its specification for Arctic latitudes.

Applying the methodology to the mapping of sediment-laden landfast ice in the southeastern Laptev Sea has yielded sediment-laden ice distribution maps consistent with field observations and our general understanding of controls on sediment entrainment into sea ice. Given the lack of data suitable for thoroughly validating this approach, results from field work conducted in a location with a uniform, homogeneous distribution of sediment-laden ice over an area constituting at least a few AVHRR pixels in size would be of great value. Despite this lack of data, this technique holds immediate potential for detecting changes in sea ice sediment loading. Additionally, measurements of the reflectance properties of a variety of ice types under a range of sediment loadings would greatly enhance the efficacy of this study. Measurements that detail the spectral reflectance properties, including BRDF, and follow the evolution of ice as it progresses through a melt season would be particularly useful.

Acknowledgements

This work has been supported through NSF RAISE grant OPP-9876843. We thank Kevin Engle for the patient and unfailing support in processing AVHRR data. Andrei Darovskikh and Andreas Schmidt helped with data processing and analysis. Satellite data were obtained through NOAA's Satellite Active Archive and the International Observatory of the North (ION) at

the University of Alaska Fairbanks. B. Light gratefully acknowledges support from the Office of Naval Research, Arctic Program under Grants N00014-97-1-0765 and N00014-03-1-0120.

References

- Antoine, D., & Morel, A. (1999). A multiple scattering algorithm for atmospheric correction of remotely sensed ocean colour (MERIS instrument): Principle and implementation for atmospheres carrying various aerosols including absorbing ones. *International Journal of Remote Sensing*, 20, 1875–1916.
- Barrie, L. (1986). Arctic air-pollution — An overview of current knowledge. *Atmospheric Environment*, 20, 643–663.
- Curry, J. A., Schramm, J. L., & Ebert, E. E. (1995). Sea ice-albedo climate feedback mechanism. *Journal of Climate*, 8, 240–247.
- Curry, J. A., Schramm, J. L., Perovich, D. K., & Pinto, J. O. (2001). Applications of SHEBA/FIRE data to evaluation of snow/ice albedo parameterizations. *Journal of Geophysical Research*, 106, 15,345–315,355.
- DeAbreu, R. A., Key, J., Maslanik, J. A., Serreze, M. C., & LeDrew, E. F. (1994). Comparison of in-situ and AVHRR-derived broad-band albedo over Arctic sea ice. *Arctic*, 47, 288–297.
- DeAbreu, R. A., Yackel, J., Marber, D., & Arkett, M. (2001). Operational satellite sensing of Arctic first-year sea ice melt. *Canadian Journal of Remote Sensing*, 27, 487–501.
- Deschamps, P. Y., Herman, M., & Tanré, D. (1983). Modeling of the atmospheric effects and its application to the remote sensing of ocean color. *Applied Optics*, 22(23), 3,751–3,758.
- Dethleff, D., Nürnberg, D., Reimnitz, E., Saarlo, M., & Savchenko, Y. P. (1993). East Siberian Arctic Region Expedition '92: The Laptev Sea — Its significance for Arctic sea ice formation and transpolar sediment flux. *Berichte zur Polarforschung*, 120, 3–37.
- Doronin, Y. P., & Kheisin, D. E. (1977). *Sea ice*. New Delhi: Amerind Publ. Co.
- Eicken, H., Kolatschek, J., Freitag, J., Lindemann, F., Kassens, H., & Dmitrenko, I. (2000). Identifying a major source area and constraints on entrainment for basin-scale sediment transport by Arctic sea ice. *Geophysical Research Letters*, 27(13), 1,919–1,922.
- Grenfell, T. C. (1983). A theoretical mode of the optical properties of sea ice in the visible and near infrared. *Journal of Geophysical Research*, 88, 9,723–9,735.
- Grenfell, T. C. (1991). A radiative transfer model for sea ice with vertical structure variations. *Journal of Geophysical Research*, 96, 16,991–17,001.
- Grenfell, T. C., Light, B., & Sturm, M. (2002). Spatial distribution and radiative effects of soot in the snow and sea ice during the SHEBA experiment. *Journal of Geophysical Research*, 107(C10), doi:10.1029/2000JC000414.
- Jin, Z. H., & Simpson, J. J. (1999). Bidirectional anisotropic reflectance of snow and sea ice in AVHRR channel 1 and 2 spectral regions — Part I: Theoretical analysis. *IEEE Transactions on Geoscience and Remote Sensing*, 37, 543–554.
- Jin, Z. H., & Simpson, J. J. (2000). Bidirectional anisotropic reflectance of snow and sea ice in AVHRR channel 1 and 2 spectral regions — Part II: Corrections applied to imagery of snow on sea ice. *IEEE Transactions on Geoscience and Remote Sensing*, 38, 999–1,015.
- Jin, Z. H., & Simpson, J. J. (2001). Anisotropic reflectance of snow observed from space over the Arctic and its effect on solar energy balance. *Remote Sensing of Environment*, 75, 63–75.
- Kolatschek, J. S. (1998). *Sea-ice dynamics and sediment transport in the Arctic: Results from field measurements, remote sensing and modeling (in German)*. Unpublished PhD, University of Bremen, Bremen.
- Liang, S., Fang, H., & Chen, M. (2001). Atmospheric correction of Landsat ETM+Land Surface Imagery — Part I: Methods. *IEEE Transactions on Geoscience and Remote Sensing*, 39(11), 2490–2498.
- Light, B., Eicken, H., Maykut, G. A., & Grenfell, T. C. (1998). The effect of included particulates in the optical properties of sea ice. *Journal of Geophysical Research*, 103, 27,739–27,752.
- Lindsay, R. W., & Rothrock, D. A. (1994). Arctic sea-ice albedo from AVHRR. *Journal of Climate*, 7, 1,737–1,749.
- Meyer, F. G., Curry, J. A., Brock, A., & Radke, L. F. (1991). Springtime visibility in the Arctic. *Journal of Applied Meteorology*, 30, 342–357.
- Nürnberg, D., Wollenburg, I., Dethleff, D., Eicken, H., Kassens, H., Letzig, T., et al. (1994). Sediments in Arctic sea ice — implications for entrainment, transport and release. *Marine Geology*, 119, 185–214.
- Osterkamp, T. E., & Gosink, J. P. (1984). *Observations and analyses of sediment-laden sea ice*. Orlando: Academic Press.
- Perovich, D. K. (1994). Light reflection from sea ice during the onset of melt. *Journal of Geophysical Research*, 99, 3,351–3,359.
- Perovich, D. K. (1998). Optical properties of sea ice. In M. Leppäranta (Ed.), *Physics of ice-covered seas* (pp. 195–230). Helsinki: University of Helsinki.
- Perovich, D. K., Grenfell, T. C., Light, B., & Hobbs, P. V. (2002). Seasonal evolution of the albedo of multiyear Arctic sea ice. *Journal of Geophysical Research*, 107(C10), 8044.
- Pfirman, S., Colony, R., Nürnberg, D., Eicken, H., & Rigor, I. (1997). Reconstructing the origin and trajectory of drifting Arctic sea ice. *Journal of Geophysical Research*, 102, 12,575–12,586.
- Pfirman, S., Lange, M. A., Wollenburg, I., Schlosser, P., Bleil, U., & Thiede, J. (1990). *Sea ice characteristics and the role of sediment inclusions in deep-sea deposition: Arctic-Antarctic comparisons* (pp. 187–211). Kluwer Academic Publishers.
- Reimnitz, E., McCormick, M., McDougall, K., & Brouwers, E. (1993). Sediment export by ice rafting from a coastal Polynya, Arctic Alaska, U.S.A. *Arctic and Alpine Research*, 25, 83–98.
- Robinson, D. A., Serreze, M. C., Barry, R. G., Scharfen, G. R., & Kukla, G. (1992). Large-scale patterns and variability of snowmelt and parameterized surface albedo in the Arctic Basin. *Journal of Climate*, 5, 1,109–1,119.
- Shaw, G. E. (1995). The Arctic Haze phenomenon. *Bulletin of the American Meteorological Society*, 76, 2403–2413.
- Stierle, A. P., & Eicken, H. (2002). Sedimentary inclusions in Alaskan coastal sea ice: Small-scale distribution, interannual variability and entrainment requirements. *Arctic, Antarctic, and Alpine Research*, 34, 103–114.
- Stroeve, J. (2001). Assessment of Greenland albedo variability from the advanced very high resolution radiometer Polar Pathfinder data set. *Journal of Geophysical Research*, 106, 33,989–34,006.
- Stroeve, J., Nolin, A., & Steffen, K. (1997). Comparison of AVHRR-derived and in situ surface albedo over the Greenland ice sheet. *Remote Sensing of Environment*, 62, 262–276.
- Sturm, B., & Zibordi, G. (2002). SeaWiFS atmospheric correction by an approximate model and vicarious calibration. *International Journal of Remote Sensing*, 23, 489–501.
- Tschudi, M. A., Curry, J. A., & Maslanik, J. A. (2001). Airborne observations of summertime surface features and their effect on surface albedo during FIRE/SHEBA. *Journal of Geophysical Research*, 106, 15,335–15,344.
- Tucker III, W. B., Gow, A. J., Meese, D. A., & Bosworth, H. W. (1999). Physical characteristics of summer sea ice across the Arctic Ocean. *Journal of Geophysical Research*, 104, 1489–1504.
- Untersteiner, N., Grantz, A., Johnson, L., & Sweeney, J. F. (1990). Structure and dynamics of the Arctic Ocean ice cover. *Geological Society of America*, 37–51.
- Vermote, E. F., Tanré, D., Deuzé, J. L., Herman, M., & Morcrette, J. J. (1997). Second simulation of the satellite signal in the solar spectrum, 6S: An overview. *IEEE Transactions on Geoscience and Remote Sensing*, 35(3), 675–685.
- Warren, S. G. (1984). Impurities in snow: Effects on albedo and snowmelt. *Annals of Glaciology*, 5, 177–179.
- Winther, J. G., Jespersen, M. N., & Liston, G. E. (2001). Blue-ice areas in Antarctica derived from NOAA AVHRR satellite data. *Journal of Glaciology*, 47, 325–334.
- Xiong, X. Z., Starnes, K., & Lubin, D. (2002). Surface albedo over the Arctic Ocean derived from AVHRR and its validation with SHEBA data. *Journal of Applied Meteorology*, 41, 413–425.